

Chiral magnetic conductivity and surface states of Weyl semimetals in topological insulator ultra-thin film multilayer

S. A. Owerre^{1,2}

¹ African Institute for Mathematical Sciences, 6 Melrose Road, Muizenberg, Cape Town 7945, South Africa.

²Perimeter Institute for Theoretical Physics, 31 Caroline St. N., Waterloo, Ontario N2L 2Y5, Canada.

E-mail: sowerre@perimeterinstitute.ca

Abstract. We investigate an ultra-thin film of topological insulator (TI) multilayer as a model for a three-dimensional (3D) Weyl semimetal. We introduce tunneling parameters t_S , t_\perp , and t_D , where the former two parameters couple layers of the same thin film at small and large momenta, and the latter parameter couples neighbouring thin film layers along the z -direction. The Chern number is computed in each topological phase of the system and we find that for $t_S, t_D > 0$, the tunneling parameter t_\perp changes from positive to negative as the system transits from Weyl semi-metallic phase to insulating phases. We further study the chiral magnetic effect (CME) of the system in the presence of a time dependent magnetic field. We compute the low-temperature dependence of the chiral magnetic conductivity and show that it captures three distinct phases of the system separated by plateaus. Furthermore, we propose and study a 3D lattice model of Porphyrin thin film, an organic material known to support topological Frenkel exciton edge states. We show that this model exhibits a 3D Weyl semi-metallic phase and also supports a 2D Weyl semi-metallic phase. We further show that this model recovers that of 3D Weyl semimetal in topological insulator thin film multilayer. Thus, paving the way for simulating a 3D Weyl semimetal in topological insulator thin film multilayer. We obtain the surface states (Fermi arcs) in the 3D model and the chiral edge states in the 2D model and analyze their topological properties.

PACS numbers: 73.43.-f, 73.43.Nq, 73.50.-h

Keywords: Weyl semimetals, Quantum anomalous conductivity, Chiral magnetic conductivity, Topological insulator thin film, Porphyrin thin film.

Submitted to: *J. Phys: Condens. Matter*

1. Introduction

Weyl semimetals are the new quantum state of matter in which a three-dimensional (3D) gapless system exhibits a nontrivial topology [1, 2, 3, 4, 5]. However, materials that host Weyl fermions in three dimensions must break either time-reversal (\mathcal{T}) or inversion (\mathcal{I}) symmetry [1, 2, 3]. This guarantees that two Weyl points separated in momentum space are topologically stable [6]. They can only annihilate each other. For isolated Weyl points, the low-energy Hamiltonian is governed by a massless Dirac equation [8, 7] $\mathcal{H}(\mathbf{k}) = \chi v_F \boldsymbol{\sigma} \cdot (\mathbf{k} - \mathbf{k}_W^\pm)$, where $\boldsymbol{\sigma}$ is the triplet Pauli matrices and \mathbf{k} is a 3-component Brillouin zone momentum and \mathbf{k}_W^\pm are the locations of the Weyl points with chirality $\chi = \pm$. Weyl points of this form are robust to external perturbation as all three Pauli matrices are used up in $\mathcal{H}(\mathbf{k})$. The chirality of the Weyl points are related to the topological charges of the system. They act as monopole and anti-monopole of the Berry curvature in the Brillouin zone (BZ) with point-like Fermi arcs surface states [7].

In recent years, several theoretical proposals of Weyl semimetals have been studied. These proposals range from pyrochlore iridates [7, 9], topological insulator (TI) multilayer [1, 2, 3, 4, 5], magnetically doped topological band insulators [10] to tight binding models [11, 12, 13, 14, 15, 16]. Recently, Weyl semimetal has been discovered experimentally in photonic crystals [17]. The experimental realization of Weyl semimetal in TaAs has also been reported using angle-resolved photoemission spectroscopy [18, 19, 20]. In a lattice model, it is possible to generate massless Dirac fermions with chirality in 2 dimensions. Such systems have been dubbed 2D Weyl semimetals [21]. They appear as chiral relativistic fermions [21] and exhibit an additional hidden discrete symmetry represented by an anti-unitary operator. The degeneracy of the resulting Weyl nodes are protected provided that there exists an anti-unitarity operator that commutes with the Hamiltonian whose square is equal to -1 at the degenerate points. This is reminiscent of time-reversal symmetry protected Dirac points in graphene.

In this paper, we study two ultra-thin film models. Firstly, we study an ultra-thin film of TI multilayer by utilizing the explicit expression of the conventional 2D TI ultra-thin film Hamiltonian [23, 24, 25, 26], which contains quadratic corrections in its low-energy Hamiltonian, with tunneling parameters t_\perp, t_S . As a customary procedure, we construct a 3D version of this model by sandwiching a normal insulator between layers of TI thin film with tunneling parameter t_D and a magnetic field along the z -direction. The resulting 3D model exhibits topological properties similar to Burkov and Balents model [1]. However, in the present model we compute the explicit expressions for the Chern numbers in all the topological phases and show that when $t_S, t_D > 0$, the tunneling parameter t_\perp changes sign as the system transits from Wely semi-metallic phase to insulating phases. We further study the low-temperature dependence of the chiral magnetic effect (CME) by computing the explicit expressions for the response function in the presence of a time-dependent magnetic field. In this case, the model

does not possess any analytical solution. We numerically show that the chiral magnetic conductivity exhibits plateaus which separate three distinct phases of the system even though it is not an integer quantized quantity.

Secondly, we study a simple lattice model using the layers of porphyrin thin films [22]— an organic material that can be synthesized in the laboratory. We present a detail analysis of this model in both 2 and 3 dimensions. In particular, we show that this lattice model captures a 2D Weyl semi-metallic phase, whose nodes are protected by an anti-unitary operator. In addition, our model also captures a 3D Weyl semi-metallic phase, which appears as an intermediate phase between a 3D quantum anomalous Hall (QAH) insulator and a normal insulator (NI). It is also shown that the porphyrin lattice model can be used as a tight binding model for topological insulator thin film multilayer. We use this model to simulate the chiral edge states of the 2D system and the surface states (Fermi arcs) of the 3D system in all the nontrivial topological phases of the system.

2. Topological insulator ultra-thin film multilayer

In 2D topological insulator ultra-thin film, the hybridization between the top and the bottom layers gives rise to a massive Dirac fermion [23, 24, 25, 26]. Here, we work from this 2D low-energy Hamiltonian and construct a 3D model for Wely semimetal by inserting insulator spacer layers between TI thin films and introduce a tunneling parameter that couples neighbouring layers of the ultra-thin film. The Hamiltonian for this multilayer is given by

$$H = \sum_{\mathbf{k}_\perp, ij} c_{\mathbf{k}_\perp i}^\dagger \mathcal{H}_{ij} c_{\mathbf{k}_\perp j}, \quad (1)$$

where

$$\begin{aligned} \mathcal{H}_{ij} = & v_F (\hat{z} \times \boldsymbol{\sigma}) \cdot \mathbf{k}_\perp \delta_{ij} + \left(\frac{t_S}{2} - t_\perp k_\perp^2 \right) \tau_z \sigma_z \delta_{ij} + \gamma \sigma_z \delta_{ij} \\ & + \frac{t_D}{2} \frac{(\delta_{j,i+1} + \delta_{j,i-1})}{2} \tau_z \sigma_z. \end{aligned} \quad (2)$$

The difference between this Hamiltonian and that of Burkov and Balents [1] is that Eq. 2 is quadratic in the momentum variables and the couplings are diagonal in the pseudo spin space. It also has an advantage in that the surface states can be simulated through a lattice model and the Chern numbers can be obtained explicitly in all the topological phases of the system.

The Pauli matrices $\boldsymbol{\sigma}$ denote the real spin space and $\boldsymbol{\tau}$ are the which surface pseudo spins; $\mathbf{k}_\perp = (k_x, k_y)$ is a 2D momentum vector in the BZ. The indices i, j label distinct thin film layers and v_F is the Fermi velocity; t_S and t_\perp are the tunneling parameters that couple the top and bottom surfaces of the same thin film layer for small k_\perp and large k_\perp respectively, and $\gamma = g\mu_B B$ is the Zeeman splitting which can be induced by magnetic doping or directly applying a magnetic field; t_D is the tunneling parameter that couples the top and bottom surfaces of neighbouring thin film layers along the growth z -direction. The parameters γ , t_\perp , t_S , and t_D depend on the thickness of the thin film, t_\perp

and t_S have been determined both numerically [24, 25, 26] and experimentally [29, 28]. The new parameter t_D can also be determined by growing the multilayer above. In the 2D model, the energy gap in the TI ultra-thin film can be enhanced by using a thinner film. Thus, the thickness of the film can change the topology of the system. In the present model, a smaller thickness should also enhance the Weyl semimetallic state induced by the interlayer coupling t_D and the magnetic field. Without loss of generality we assume all the parameters to be positive $b, t_S, t_D > 0$. However, as will be shown in the subsequent sections, t_\perp can be positive or negative when moving from the Weyl semi-metallic phase to other phases of the system.

It is expedient to Fourier transform the Hamiltonian along the growth z -direction. We obtain

$$\mathcal{H}(\mathbf{k}) = v_F(\hat{z} \times \boldsymbol{\sigma}) \cdot \mathbf{k}_\perp + [\gamma + \hat{\Delta}(\mathbf{k})]\sigma_z, \quad (3)$$

where

$$\hat{\Delta}(\mathbf{k}) = \left[\frac{t_S}{2} - t_\perp k_\perp^2 + \frac{t_D}{2} \cos(k_z d) \right] \tau_z. \quad (4)$$

The Hamiltonian (Eq. 3) breaks \mathcal{T} -symmetry due to the magnetic field, but inversion symmetry is preserved $\mathcal{I} : \mathcal{H}(\mathbf{k}) \rightarrow \tau_z \sigma_z \mathcal{H}(-\mathbf{k}) \tau_z \sigma_z$. The eigenvalues of $\hat{\Delta}(\mathbf{k})$ are $\pm \Delta(\mathbf{k})$, where $\Delta(\mathbf{k}) = \frac{t_S}{2} - t_\perp k_\perp^2 + \frac{t_D}{2} \cos(k_z d)$ and the corresponding eigenspinors are

$$|u^\uparrow\rangle = \begin{pmatrix} 1 \\ 0 \end{pmatrix}; \quad |u^\downarrow\rangle = \begin{pmatrix} 0 \\ 1 \end{pmatrix}. \quad (5)$$

Hence, the Hamiltonian can be written as a 2×2 massless Dirac equation (Weyl equations) given by

$$\mathcal{H}_s(\mathbf{k}) = v_F(\hat{z} \times \boldsymbol{\sigma}) \cdot \mathbf{k}_\perp + m_s(\mathbf{k})\sigma_z, \quad (6)$$

with $m_s(\mathbf{k}) = \gamma + s\Delta(\mathbf{k})$ and $s = \pm$ or \uparrow, \downarrow . The form of the $\hat{\Delta}$ function for this model affects the phases that emerged when $\gamma = 0$. For the present model, Eq. 6 with $\gamma = 0$ describes a 3D Dirac semimetal which possesses time-reversal and inversion symmetries. It exhibits a phase with two Dirac nodes along the k_z -direction when $t_S < t_D$ and an insulating phase (3D QSH phase) for $t_S > t_D$. In the insulating phase, the Z_2 topological number is $(-1)^\nu = -\text{sign}(t_S - t_D)$, where $\nu = 1$ characterizes a nontrivial phase. The semi-metallic phase and the insulating phase are separated by a saddle point at $k_x = k_y = 0$, $k_z = \pi/d$, with energy $\pm |t_S - t_D|/2$.

To obtain a nontrivial Weyl semi-metallic phase, \mathcal{T} - or \mathcal{I} -symmetry must be broken as mentioned above. This requires that $\gamma \neq 0$. The corresponding energy eigenvalues of Eq. 6 are given by

$$\epsilon_{s\lambda}(\mathbf{k}) = \lambda \sqrt{v_F^2 k_\perp^2 + m_s^2(\mathbf{k})} = \lambda \epsilon_s(\mathbf{k}), \quad (7)$$

where $\lambda = \pm$ labels the conduction and the valence bands respectively, and the eigenvectors are

$$|v_{\mathbf{k}}^{\lambda s}\rangle = \frac{1}{\sqrt{2}} \begin{pmatrix} \sqrt{1 + \lambda \frac{m_s(\mathbf{k})}{\epsilon_s(\mathbf{k})}}, -i\lambda e^{i\phi_{\mathbf{k}_\perp}} \sqrt{1 - \lambda \frac{m_s(\mathbf{k})}{\epsilon_s(\mathbf{k})}} \end{pmatrix}^T, \quad (8)$$

where $e^{i\phi_{\mathbf{k}_\perp}} = (k_x + ik_y)/k_\perp$. Hence, the eigenspinors of the complete system are $|\psi_{\mathbf{k}}^{\lambda s}\rangle = |u^s\rangle \otimes |v_{\mathbf{k}}^{\lambda s}\rangle$, where

$$|\psi_{\mathbf{k}}^{\uparrow\lambda}\rangle = \begin{pmatrix} |v_{\mathbf{k}}^{\uparrow\lambda}\rangle \\ \mathbf{0} \end{pmatrix}; \quad |\psi_{\mathbf{k}}^{\downarrow\lambda}\rangle = \begin{pmatrix} \mathbf{0} \\ |v_{\mathbf{k}}^{\downarrow\lambda}\rangle \end{pmatrix}. \quad (9)$$

Two Weyl nodes are realized in the $\mathcal{H}_\downarrow(\mathbf{k})$ block of the Dirac equation (Eq. 6). This corresponds to the solutions of $m_\downarrow(\mathbf{k}) = 0$, where $m_\uparrow(\mathbf{k})$ never changes sign. The Weyl nodes are located at $k_x = k_y = 0$, $k_z^\pm = \pi/d \pm k_W$, where

$$k_W = \frac{1}{d} \arccos \left(1 - \frac{2}{t_D} (\gamma - \gamma_-) \right), \quad (10)$$

with $\gamma_\pm = (t_S \pm t_D)/2$ and $\gamma_+ > \gamma_-$.

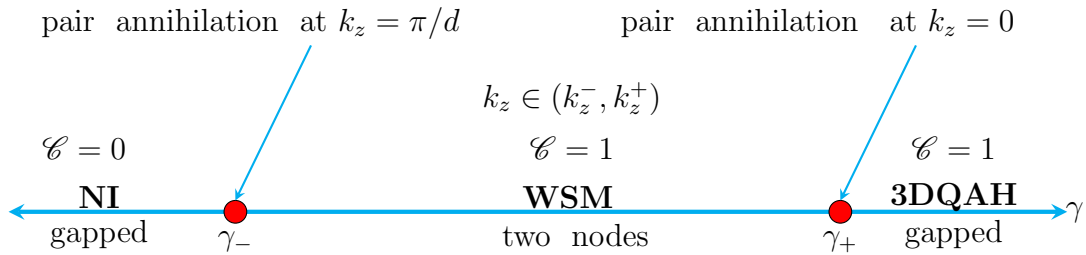


Figure 1. Color online. The phase diagram of the TI multilayer comprising a normal insulator (NI), Weyl semimetal (WSM), and quantum anomalous Hall (QAH) insulator along the magnetic field line. The values of the corresponding Chern numbers are indicated by \mathcal{C} .

The phase diagram in Fig. 1 comprises an ordinary insulator phase for $\gamma < \gamma_-$, and a 3D QAH phase for $\gamma > \gamma_+$. A 3D Weyl semimetal with two Weyl nodes appears in the regime $\gamma_- < \gamma < \gamma_+$, and a pair annihilation occurs exactly at the boundaries. As in all theoretical models, a 3D Weyl semimetal phase always appears as an intermediate state between an ordinary insulator and a 3D quantum anomalous Hall insulator. The Hall conductivity is given by

$$\sigma_{xy}^s(k_z) = \frac{e^2}{h} \mathcal{C}^s(k_z). \quad (11)$$

In the present model, we can calculate the Chern number explicitly by treating k_z as a parameter, thus reducing the problem to an effective 2D model. Hence, the Chern number is computed with the same formula [27]

$$\mathcal{C}^s(k_z) = \int dk_\perp \frac{\partial \mathcal{A}_{\phi_{\mathbf{k}_\perp}}^s}{\partial k_\perp}, \quad (12)$$

where

$$\mathcal{A}_{\phi_{\mathbf{k}_\perp}}^s = i \langle \psi_-^s | \partial_{\phi_{\mathbf{k}_\perp}} \psi_-^s \rangle. \quad (13)$$

The $s = \downarrow (-)$ block realizes Weyl nodes, therefore the Chern number is defined only for the occupied band of this block. Using Eqs. 12 and 13 we obtain

$$\mathcal{C}^\downarrow(k_z) = -\frac{1}{2} [\text{sign}(\tilde{m}_\downarrow(k_z)) - \text{sign}(t_\perp)], \quad (14)$$

where $\tilde{m}_\downarrow(k_z) = \gamma - \left(\frac{t_S}{2} + \frac{t_D}{2} \cos(k_z d)\right)$.

In the Weyl semi-metallic phase $\gamma_- < \gamma < \gamma_+$, k_z must take values in-between the nodes, i.e., $k_z \in (k_z^-, k_z^+)$, hence $\tilde{m}_\downarrow(k_z) < 0$. A nonzero Chern number then requires $t_\perp > 0$. The Chern number only changes when the gap closes and reopens at the boundaries $\gamma = \gamma_\pm$. Once the gap closes and reopens we must have $t_\perp < 0$ to get a normal insulator phase and a nontrivial 3D QAH phase at $k_z = \pi/d$ and $k_z = 0$ respectively (see Fig. 1). This can be explicitly shown by evaluating the Chern number at $k_z = 0$ where the gap closes and reopens for $\gamma > \gamma_+$. We obtain

$$\mathcal{C}^\downarrow(0) = -\frac{1}{2}[\text{sign}(\gamma - \gamma_+) - \text{sign}(t_\perp)]. \quad (15)$$

A similar situation occurs at $k_z = \pi/d$ for $\gamma < \gamma_-$, and the Chern number is given by

$$\mathcal{C}^\downarrow\left(\frac{\pi}{d}\right) = -\frac{1}{2}[\text{sign}(\gamma - \gamma_-) - \text{sign}(t_\perp)]. \quad (16)$$

Note that Eqs. 15 and 16 reduce to the 2D Chern number [23] when $\gamma = t_D = 0$. In this case, the band inversion requires that $t_\perp t_S > 0$ for a nontrivial topological phase to exist. For $\gamma \neq 0$, the present model requires that $t_\perp < 0$ as mentioned above. This guarantees that the first Chern number, Eq. 15, is integer quantized and describes a 3D QAH phase and the second Chern number, Eq. 16, is zero which describes a normal insulator phase. As mentioned above, the topological property of Weyl semimetal is also manifested as monopoles and anti-monopoles of the Berry curvature. This is evident by expanding Eq. 14 near the Weyl nodes, we obtain

$$\mathcal{C}^\downarrow(k_z) = \chi \tilde{v}_F \text{sign}(k_z - k_z^\pm) + \dots \quad (17)$$

where $\tilde{v}_F = t_D d \sin(k_W d)/4$, and $\chi = \pm$ is the chirality of the Weyl nodes. This expression explicitly shows a monopole and anti-monopole at $k_z = k_z^\pm$ with chirality $\chi = \pm$ respectively.

The Fermi arcs in the vicinity of the Weyl nodes is a special feature of Weyl semimetals. These arcs are exactly the edge states of the effective 2D system for fixed k_z , and exist for any surface not perpendicular to the z -axis [1]. We can explicitly solve for these edge states by considering a slab geometry occupying the half-plane $x \geq 0$ with open boundary condition along x -direction and translational invariant in the y - z plane. Thus, k_y and k_z are good quantum numbers and k_x is replaced by $k_x \rightarrow -i\partial_x$. The Hamiltonian can be written as

$$H_- = i\sigma_y v_F \partial_x - \sigma_z t_\perp \partial_x^2 + v_F \sigma_x k_y - \sigma_z t_\perp k_y^2 + m_-(k_z, x) \sigma_z. \quad (18)$$

We first consider $k_y = 0$ and solve for the zero energy solution of the Schrödinger equation $\mathcal{H}_- \Phi(k_z, x) = 0$,

$$[v_F \partial_x + t_\perp \sigma_x \partial_x^2 - m_-(k_z, y) \sigma_x] \Phi(k_z, x) = 0, \quad (19)$$

where $\Phi(k_z, x)$ is a 2-component spinor and we have multiplied through by $-i\sigma_y$. We seek for a solution of the form

$$\Phi_\lambda(k_z, x) = \xi_\lambda e^{\omega x}, \quad (20)$$

where $\sigma_x \xi_\lambda = \lambda \xi_\lambda$, ($\lambda = \pm 1$) and ω solves the equation

$$v_F \omega + \lambda t_\perp \omega^2 - \lambda m_-(k_z, x) = 0. \quad (21)$$

The allowed solution that obey the boundary conditions of the wavefunction [$\Phi(k_z, 0) = \Phi(k_z, \infty) = 0$] is given by

$$\Phi_\lambda(k_z, x) = \frac{\mathcal{C}}{\sqrt{2}} \begin{pmatrix} 1 \\ \lambda \end{pmatrix} (e^{-\omega_+ x} - e^{-\omega_- x}), \quad (22)$$

where \mathcal{C} is a normalization constant, and ω_\pm are the positive solutions of Eq. 21. The surface Hamiltonian is obtained by projecting Eq. 18 onto the surface states

$$\mathcal{H}_{sur}(k_y, k_z) = \Phi_\lambda^\dagger \mathcal{H}_- \Phi_\lambda = v_F k_y \sigma_z. \quad (23)$$

3. Magnetic field response

In the previous section, we derived the phase diagram, anomalous Hall conductivity, and surface states of an ultra-thin film of TI Hamiltonian with quadratic momentum corrections. In this section, we study the response of the system to an orbital magnetic field through the vector potential, $\mathbf{A} = x \mu_B B \hat{y}$, which corresponds to a magnetic field along the growth z -direction. The Hamiltonian is given by

$$\mathcal{H}_s(\mathbf{k}) = v_F (\hat{z} \times \boldsymbol{\sigma}) \cdot (-i \nabla + e \mathbf{A}) + m_s(\mathbf{k}) \sigma_z. \quad (24)$$

We introduce the operator $\boldsymbol{\pi} = -i \nabla + e \mathbf{A}$, and define the creation and annihilation operators: $a = l_B (\pi_x - i \pi_y) / \sqrt{2}$; $a^\dagger = l_B (\pi_x + i \pi_y) / \sqrt{2}$, where $l_B^2 = (e \mu_B B)^{-1}$ is the magnetic length. In terms of a and a^\dagger the Hamiltonian becomes

$$\mathcal{H}_s(k_z) = i \omega_B \sqrt{2} (\sigma^+ a - \sigma^- a^\dagger) + m_s(k_z) \sigma_z, \quad (25)$$

where $\sigma^\pm = (\sigma_x \pm i \sigma_y) / 2$ and $m_s(k_z) = \gamma + s \Delta(k_z)$, where $\Delta(k_z)$ is given by

$$\Delta(k_z) = \left[\frac{t_S}{2} + \frac{t_D}{2} \cos(k_z d) - \omega_0 \left(a^\dagger a + \frac{1}{2} \right) \right]. \quad (26)$$

Here, $\omega_B = v_F / l_B$ is the magnetic frequency and $\omega_0 = 2 t_\perp / l_B^2$ is the harmonic oscillator frequency. The eigenvector of each 2×2 block may be written as

$$\mathcal{U}_{sn} = \begin{pmatrix} \alpha_{sn}^1 u_{n-1} \\ \alpha_{sn}^2 u_n \end{pmatrix}, \quad (27)$$

where $\alpha_{sn}^1, \alpha_{sn}^2$ are constants to be determined. The operators satisfy $a u_n = \sqrt{n} u_{n-1}$; $a^\dagger u_n = \sqrt{n+1} u_{n+1}$. Hence, Eq. 25 yields a 2×2 eigenvalue equation for α_{sn} . The Hamiltonian yields

$$\mathcal{H}_{sn}(k_z) = s \frac{\omega_0}{2} \sigma_0 - \omega_B \sqrt{2n} \sigma_y + m_{sn}(k_z) \sigma_z, \quad (28)$$

where σ_0 is an identity matrix, $m_{sn}(k_z) = \gamma + s \Delta_n(k_z)$, and

$$\Delta_n(k_z) = \frac{t_S}{2} + \frac{t_D}{2} \cos(k_z d) - \omega_0 n. \quad (29)$$

The eigenvalues of Eq. 28 are given by

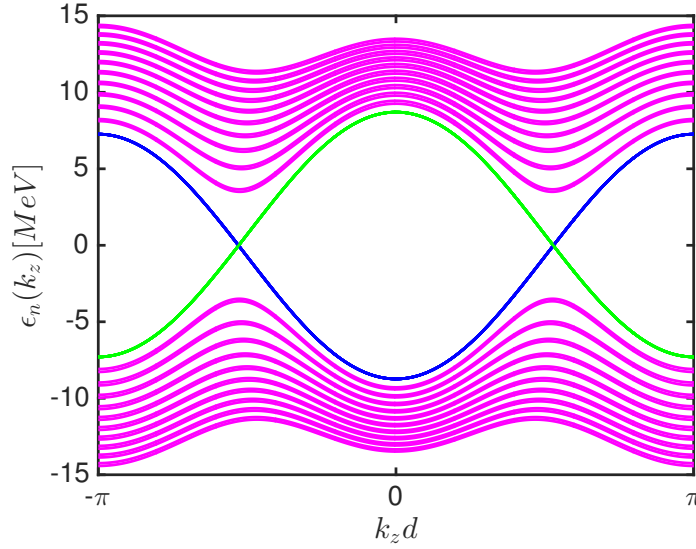


Figure 2. Color online. The Landau levels as a function of the momentum $k_z d$. The parameters are $\mu_B B = 0.1\text{T}$; $t_S = 1\text{MeV}$, $t_D = 10\text{MeV}$, $v_F = 500\text{MeV}$; $g = 0.1\text{MeV}$.

$$\epsilon_{n,\lambda}^s(k_z) = s \frac{\omega_0}{2} + \lambda \sqrt{2n\omega_B^2 + m_{sn}^2(k_z)}, \quad n \geq 1, \quad (30)$$

$$\epsilon_0^s(k_z) = s \frac{\omega_0}{2} - m_{s,0}(k_z), \quad n = 0. \quad (31)$$

The corresponding eigenvectors are

$$|v_n^{\lambda s}\rangle = \frac{1}{\sqrt{2}} \left(\sqrt{1 + \lambda \frac{m_{sn}(k_z)}{\tilde{\epsilon}_n^s(k_z)}}, -i\lambda \sqrt{1 - \lambda \frac{m_{sn}(k_z)}{\tilde{\epsilon}_n^s(k_z)}} \right)^T, \quad (32)$$

$$|v_0^s\rangle = (0, 1)^T, \quad (33)$$

where $\tilde{\epsilon}_{n\lambda}^s(k_z) = \epsilon_{n\lambda}^s(k_z) + s\omega_0/2$. The eigenspinors of the complete system are $|\psi^{s\lambda}\rangle = |u^s\rangle \otimes |v_n^{s\lambda}\rangle$, where

$$|\psi_n^{\uparrow\lambda}\rangle = \begin{pmatrix} |v_n^{\uparrow\lambda}\rangle \\ \mathbf{0} \end{pmatrix} \quad \text{and} \quad |\psi_n^{\downarrow\lambda}\rangle = \begin{pmatrix} \mathbf{0} \\ |v_n^{\downarrow\lambda}\rangle \end{pmatrix}. \quad (34)$$

For $\gamma = 0$, the zero Landau levels crosses at $B_c = (t_S + t_D \cos(k_z d))/2e\mu_B t_\perp$, which vanishes at the Dirac nodes $k_z^\pm = \pi/d \pm k_W$. At the transition point $k_z = \pi/d$, $B_c \neq 0$. For $t_S > t_D$, the regime $B < B_c$ corresponds to a 3D QSH phase and $B > B_c$ corresponds to trivial phase. The Landau level for $\gamma \neq 0$ is shown in Fig. 2, which evidently captures the appearance of two Weyl nodes in the vicinity of the bulk gap.

3.1. Chiral magnetic effect

Chiral magnetic effect is the response of a system to a time-dependent magnetic field. This phenomenon is well-known in high energy physics as the chiral magnetic conductivity. For instance, gluon field configurations with nonzero topological charges

exhibit this effect [34]. It has been shown to occur in Weyl semimetals [5, 33]. In this subsection, we investigate the low-temperature dependence of the chiral magnetic conductivity on the TI ultra-thin film Hamiltonian. We will derive the expressions for our model, which do not possess any analytical solution. We also show that the chiral magnetic conductivity captures the appearance of the three distinct phases of the system though it is not integer quantized like the quantum anomalous Hall conductivity. In the linear response theory, the current operator is given by

$$J^i(\mathbf{q}, \omega) = \Pi_{ij}(\mathbf{q}, \omega) A^j(\mathbf{q}, \omega), \quad (35)$$

where $\Pi_{ij}(\mathbf{q}, \omega)$ is the current-current correlation function. The chiral magnetic effect (or conductivity) arises in the presence of a time-dependent magnetic field along the z -direction. In the Landau gauge we adopt here, the magnetic field is only related to the A_y component of the gauge field, that is $B_z = \partial_x A_y(x)$. Assuming $A_y(x) = A(\mathbf{q}, \omega) e^{i(qx - \omega t)}$, we have $B_z(\mathbf{q}, \omega) = iqA(\mathbf{q}, \omega)$. The response of the system to a time-dependent magnetic field gives rise to an induced current given by

$$J(\mathbf{q}, \omega) = \sigma_\chi(\mathbf{q}, \omega) B_z(\mathbf{q}, \omega). \quad (36)$$

Thus, the chiral magnetic conductivity is

$$\sigma_\chi(\mathbf{q}, \omega) = \frac{-i}{q} \Pi(\mathbf{q}, \omega). \quad (37)$$

The response function $\Pi(\mathbf{q}, \omega)$ is in general antisymmetric. The most convenient way to calculate the response function is from the imaginary time path integral of Eq. 24 minimally coupled to a vector potential,

$$\mathcal{S} = \int d\tau d^3r \psi^\dagger(\mathbf{r}, \tau) \left[\partial_\tau - \mu + ieA_0(\mathbf{r}, \tau) + \mathcal{H}_s \right] \psi(\mathbf{r}, \tau). \quad (38)$$

After integrating out the fermion degree of freedom, the response function is given by [33]

$$\begin{aligned} -i\Pi(\mathbf{q}, i\Omega) &= i \frac{e^2 v_F}{V} \sum_{ss'; \lambda\lambda'} \sum_{\mathbf{k}} \frac{f[\xi_{s'\lambda'}(\mathbf{k})] - f[\xi_{s\lambda}(\mathbf{k} + \mathbf{q})]}{i\Omega + \xi_{s'\lambda'}(\mathbf{k}) - \xi_{s\lambda}(\mathbf{k} + \mathbf{q})} \\ &\quad \times \langle \psi_{\mathbf{k}+\mathbf{q}}^{s\lambda} | \psi_{\mathbf{k}}^{s'\lambda'} \rangle \langle \psi_{\mathbf{k}}^{s'\lambda'} | \boldsymbol{\sigma} \cdot \mathbf{q} | \psi_{\mathbf{k}+\mathbf{q}}^{s\lambda} \rangle, \end{aligned} \quad (39)$$

where $i\Omega = \omega + i\eta$ and $f[\xi_{s\lambda}(\mathbf{k})] = [e^{\xi_{s\lambda}(\mathbf{k})/T} + 1]^{-1}$ is the Fermi function, with $\xi_{s\lambda}(\mathbf{k}) = \epsilon_{s\lambda}(\mathbf{k}) - \epsilon_F$. Without loss of generality we assume $\epsilon_F > 0$. The spatial contribution only comes from the Landau gauge choice, thus we take $\mathbf{q} = q\hat{x}$. There are two contributions to the response function — the interband with $\lambda \neq \lambda'$ and the intraband with $\lambda = \lambda'$. We are interested in the low-frequency and long wavelength limits $i\Omega \rightarrow 0$ (*second limit*); $q \rightarrow 0$ (*first limit*) and $q \rightarrow 0$ (*second limit*); $i\Omega \rightarrow 0$ (*first limit*). However, the two limits are not commutative so the order in which the limits are taken is very crucial. The former limit is the direct current (DC) limit of a transport coefficient, while the latter is the static limit. For the interband case, both order of limits contribute to the response function, so we can start with $i\Omega = 0$. In this case all other terms in Eq. 39 are finite as $q = 0$ except $\langle \psi_{\mathbf{k}+\mathbf{q}}^{s\lambda} | \psi_{\mathbf{k}}^{s'\lambda'} \rangle$. Hence, we will expand this term to first

order in q . Since the pseudo spin scalar product produces a term $\langle u^s | u^{s'} \rangle = \delta_{ss'}$, we have

$$\begin{aligned} \langle \psi_{\mathbf{k}+\mathbf{q}}^{s\pm} | \psi_{\mathbf{k}}^{s'\mp} \rangle &= \delta_{ss'} \frac{q}{2v_F k_{\perp} \epsilon_s^2(\mathbf{k})} \left[\pm 2k_x t_{\perp} m_s^2(\mathbf{k}) \right. \\ &\quad \left. + v_F^2 (-ik_y \epsilon_s(\mathbf{k}) \mp k_x m_s(\mathbf{k})) \right], \end{aligned} \quad (40)$$

$$\langle \psi_{\mathbf{k}}^{s'\pm} | \psi_{\mathbf{k}}^{s\mp} \rangle = \delta_{ss'} \frac{1}{k_{\perp}} [-k_y \frac{\epsilon_s(\mathbf{k})}{m_s(\mathbf{k})} \pm ik_x]. \quad (41)$$

Plugging Eqs. 40 and 41 into Eq. 39, the terms containing $k_x k_y$ vanish by angular integration, we obtain

$$-i\Pi^{inter}(\mathbf{q}, i\Omega) = \frac{e^2 q}{2} \sum_s \int \frac{d\mathbf{k}}{(2\pi)^3} \frac{1 - f[\epsilon_s(\mathbf{k}) - \epsilon_F]}{\epsilon_s^3(\mathbf{k})} M_s(\mathbf{k}), \quad (42)$$

where

$$M_s(\mathbf{k}) = v_F^2 m_s(\mathbf{k}) - 2 \frac{k_x^2}{k_{\perp}^2} t_{\perp} m_s^2(\mathbf{k}). \quad (43)$$

Performing the angular integration, we obtain

$$\begin{aligned} -i\Pi^{inter}(\mathbf{q}, i\Omega) &= -\frac{e^2 q}{8\pi^2} \sum_s \int_{-\pi/d}^{\pi/d} dk_z \int_0^{\infty} dx [\Omega_{1z}^s(x, k_z) + \Omega_{2z}^s(x, k_z)] \\ &\quad \times [1 - f(\sqrt{x + m_s^2(x, k_z)} - \epsilon_F)], \end{aligned} \quad (44)$$

where $x = v_F^2 k_{\perp}^2$ and

$$\begin{aligned} \Omega_{1z}^s(x, k_z) &= -\frac{m_s(x, k_z)}{2[x + m_s^2(x, k_z)]^{3/2}}, \\ \Omega_{2z}^s(x, k_z) &= \frac{\tilde{t}_{\perp} m_s^2(x, k_z)}{2[x + m_s^2(x, k_z)]^{3/2}}, \\ m_s(x, k_z) &= \gamma + s \left[\frac{t_S}{2} - \tilde{t}_{\perp} x + \frac{t_D}{2} \cos(k_z d) \right], \end{aligned} \quad (45)$$

with $\tilde{t}_{\perp} = t_{\perp}/v_F^2$. Now for the intraband case $\lambda = \lambda'$, the response function vanishes in the DC limit $i\Omega \rightarrow 0$; $q \rightarrow 0$, i.e., if we take long-wavelength limit first. However, in the static limit $q \rightarrow 0$, $i\Omega \rightarrow 0$, it is nonzero. In this case, we have

$$f[\xi_{s\lambda}(\mathbf{k} + \mathbf{q})] = f[\xi_{s\lambda}(\mathbf{k})] + \mathbf{q} \frac{\partial \xi_{s\lambda}(\mathbf{k})}{\partial \mathbf{q}} \frac{\partial f[\xi_{s\lambda}(\mathbf{k})]}{\partial \xi_{s\lambda}(\mathbf{k})} + \dots \quad (46)$$

$$\xi_{s\lambda}(\mathbf{k} + \mathbf{q}) = \xi_{s\lambda}(\mathbf{k}) + \mathbf{q} \frac{\partial \xi_{s\lambda}(\mathbf{k})}{\partial \mathbf{q}} + \dots \quad (47)$$

The intraband response function is given by

$$-i\Pi^{intra}(\mathbf{q}, i\Omega) = \frac{e^2 q}{2} \sum_s \int \frac{d\mathbf{k}}{(2\pi)^3} \left(-\frac{\partial f[\xi_{s\lambda}(\mathbf{k})]}{\partial \xi_{s\lambda}(\mathbf{k})} \right) \frac{M_s(\mathbf{k})}{\epsilon_s^2(\mathbf{k})}. \quad (48)$$

In the present model, the integrations [Eqs. 44 and 48] cannot be done analytically. We can reduce the problem in a way that is amenable to numerical integration by performing

the angular integration. We obtain

$$\begin{aligned}
 -i\Pi^{intra}(\mathbf{q}, i\Omega) &= -\frac{e^2 q}{8\pi^2} \sum_s \int_{-\pi/d}^{\pi/d} dk_z \int_0^\infty dx [\tilde{\Omega}_{1z}^s(x, k_z) + \tilde{\Omega}_{2z}^s(x, k_z)] \\
 &\quad \times \left[4T \cosh^2 \left(\sqrt{x + m_s^2(x, k_z)} - \epsilon_F \right) \right]^{-1}, \quad (49)
 \end{aligned}$$

where

$$\tilde{\Omega}_{1z}^s(x, k_z) = -\frac{m_s(x, k_z)}{2[x + m_s^2(x, k_z)]}; \quad \tilde{\Omega}_{2z}^s(x, k_z) = \frac{\tilde{t}_\perp m_s^2(x, k_z)}{2[x + m_s^2(x, k_z)]}. \quad (50)$$

The conductivity is given by Eq. 37. In the two non-commutative limits we obtain two conductivities given by

$$\sigma_\chi = \lim_{\Omega \rightarrow 0} \lim_{q \rightarrow 0} \frac{-i}{q} \Pi^{inter}(\mathbf{q}, i\Omega), \quad (51)$$

$$\sigma_t = \lim_{q \rightarrow 0} \lim_{\Omega \rightarrow 0} \frac{-i}{q} [\Pi^{inter}(\mathbf{q}, i\Omega) + \Pi^{intra}(\mathbf{q}, i\Omega)]. \quad (52)$$

The first limit [Eq. 51] is the chiral magnetic effect (CME). As mentioned above, this is nothing but the chiral magnetic conductivity, a phenomenon well-studied in high energy physics [34]. The second limit [Eq. 52] is a thermodynamic equilibrium quantity corresponding to the static limit; we will focus on Eq. 51.

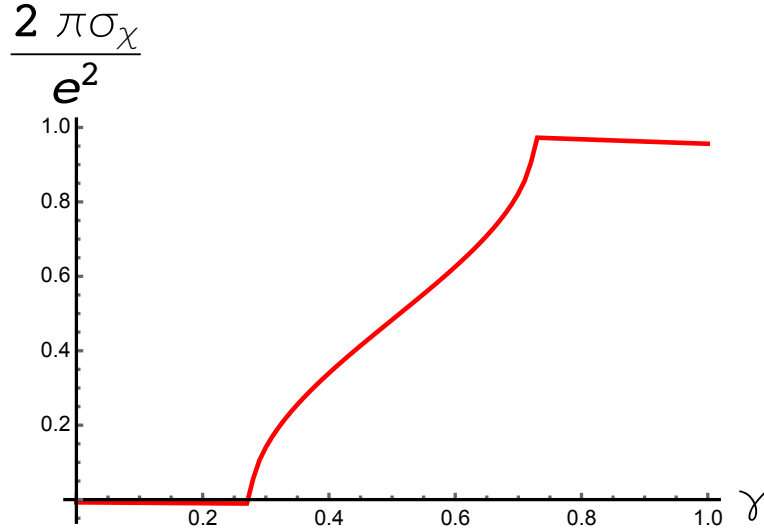


Figure 3. Color online. The chiral magnetic conductivity as a function of γ at $\epsilon_F = 0$ and $T = 0.001$ in units of t_S . The parameters are $t_D = 0.45t_S$ and $t_\perp = 0.01t_S$. The sign of t_\perp is unimportant because m_\pm contribute to σ_χ . The different regimes separated by plateaus are ordinary insulator $\gamma < \gamma_-$ ($\sigma_\chi = 0$); Weyl semimetal $\gamma_- < \gamma < \gamma_+$ ($\sigma_\chi \neq 0$), and quantum anomalous Hall insulator $\gamma > \gamma_+$ ($\sigma_\chi \neq 0$).

Figure 3 shows the plot of the chiral magnetic conductivity against the magnetic field γ . Note that the sign of t_\perp is irrelevant because the two masses $m_\pm(\mathbf{k})$ contribute in the computation of chiral magnetic conductivity. Interestingly, the chiral magnetic conductivity captures the appearance of the three phases of the system. The plateaus

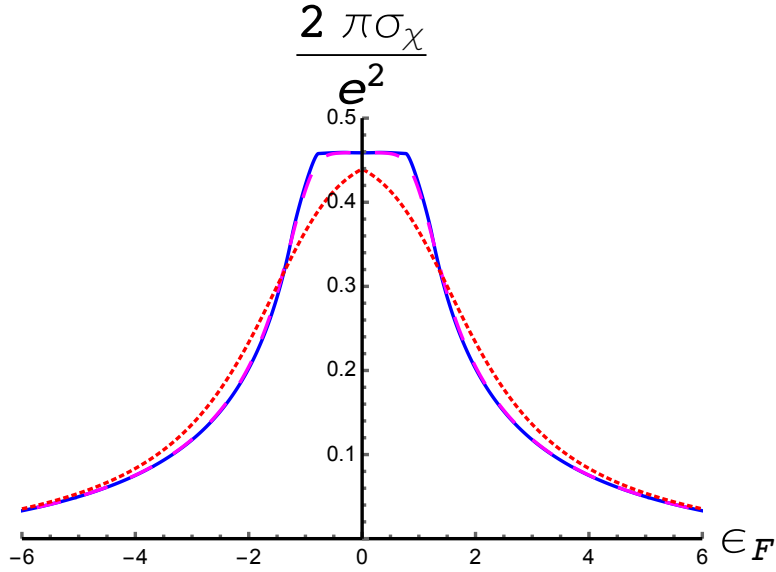


Figure 4. Color online. The chiral magnetic conductivity as a function of the Fermi energy for several temperatures $T = 0.001$ (solid); $T = 0.1$ (dashed); $T = 0.5$ (dotted). The parameters are in units of t_S with $t_D = 0.45t_S$; $t_{\perp} = 0.01t_S$, $v_F = 1$; $\gamma_- < \gamma = 0.5t_S < \gamma_+$.

of σ_{χ} correspond to phase transitions from ordinary insulator $\gamma < \gamma_-$ ($\sigma_{\chi} = 0$) to Weyl semimetal $\gamma_- < \gamma < \gamma_+$ ($\sigma_{\chi} \neq 0$), and from Weyl semimetal to quantum anomalous Hall insulator $\gamma > \gamma_+$ ($\sigma_{\chi} \neq 0$). Also notice from Fig. 3 that the chiral magnetic conductivity is not a quantized quantity unlike the quantum anomalous Hall conductivity, Eq. 11. Figure 4 shows the chiral magnetic conductivity as a function of the Fermi energy. In this case, a step peak occurs at $\epsilon_F = 0$ at low temperatures.

4. Porphyrin thin film multilayer

In this section, we propose and analyze a lattice model for Weyl semimetals from a porphyrin thin film layer. We will also show the connection of this model to that of TI thin film studied above. To construct a 3D lattice model, it is customary to stack layers of porphyrin thin film on top of each other along the z -direction. The 2D Hamiltonian of a porphyrin thin film is given by [22]

$$\begin{aligned}
 H_{2D} = & \sum_{m,\alpha} \left[\mathcal{J}_1 (e^{i\Phi} a_m^\dagger b_{m+\hat{\delta}_\alpha} + e^{-i\Phi} a_m^\dagger b_{m-\hat{\delta}_\alpha}) \right. \\
 & \left. + \mathcal{J}_2 (e^{-i\Phi} a_m^\dagger b_{m+\hat{\delta}_\alpha} + e^{i\Phi} a_m^\dagger b_{m-\hat{\delta}_\alpha}) + h.c. \right] \\
 & + J_{\perp} \sum_m [a_m^\dagger a_{m+\hat{x}(\hat{y})} - b_m^\dagger b_{m+\hat{x}(\hat{y})} + h.c.] + \mu_{xy} \sum_m [a_m^\dagger a_m - b_m^\dagger b_m]. \quad (53)
 \end{aligned}$$

The nearest neighbour (NN) sites are along the diagonals with coordinates $\hat{\delta}_1 = (\hat{x} + \hat{y})/2$ and $\hat{\delta}_2 = (-\hat{x} + \hat{y})/2$, and complex hopping parameters, \mathcal{J}_l , where $l = 1, 2$; $\hat{x} = (1, 0)$

and $\hat{y} = (0, 1)$; Φ is a phase factor, which can be regarded as a magnetic flux treading the lattice. The total flux on a square plaquette vanishes just like in Haldane model [30]. The next nearest neighbour (NNN) sites are along the horizontal and vertical axes with real hopping parameter J_{\perp} . The last term in Eq. 53 is the staggered onsite potential with a tuneable parameter μ_{xy} .

Next, we introduce an interlayer coupling between the porphyrin thin film layers along the z -direction. The Hamiltonian is given by

$$H_{inter} = J_D \sum_m [a_m^\dagger a_{m+\hat{z}} - b_m^\dagger b_{m+\hat{z}} + h.c.] + \mu_z \sum_m [a_m^\dagger a_m - b_m^\dagger b_m]. \quad (54)$$

Here, the staggered onsite potential is along the z -direction with tuneable parameter μ_z , and J_D is a real coupling constant. Performing the Fourier transform of the lattice model we obtain $\mathcal{H} = \sum_{\mathbf{k}} (a_{\mathbf{k}}^\dagger, b_{\mathbf{k}}^\dagger) \mathcal{H}(\mathbf{k}) (a_{\mathbf{k}}, b_{\mathbf{k}})^T$, where

$$\begin{aligned} \mathcal{H}(\mathbf{k}) = & [\rho_1 \cos(k_+ - \Phi) + \rho_2 \cos(k_- + \Phi)] \sigma_x \\ & - [\tilde{\rho}_1 \cos(k_+ - \Phi) + \tilde{\rho}_2 \cos(k_- + \Phi)] \sigma_y \\ & + [\mu_{xy} - 2t_{\perp} (\cos(k_+ + k_-) + \cos(k_+ - k_-))] \sigma_z \\ & - \frac{t_D}{2} [\cos(k_z d) + \cos(k_W d)] \sigma_z; \end{aligned} \quad (55)$$

The above Hamiltonian Eq. 55 is obtained with the rescaled parameters $J_{\perp} \rightarrow -t_{\perp}$, $J_D \rightarrow -t_D/4$, and we have fine-tuned the staggered potential to $\mu_z = J_D \cos(k_W d)$. We also set the lattice constants $a_x = a_y = 1$, and $a_z = d$, where d is the separation of the porphyrin thin film layers. $k_{\pm} = (k_x \pm k_y)/2$, $\rho_1 = 2\mathcal{R}\mathcal{J}_1$, $\rho_2 = 2\mathcal{R}\mathcal{J}_2$; $\tilde{\rho}_1 = 2\mathcal{I}\mathcal{J}_1$, and $\tilde{\rho}_2 = 2\mathcal{I}\mathcal{J}_2$, where \mathcal{R} and \mathcal{I} denote real and imaginary parts of the complex hopping terms $\mathcal{J}_{1,2}$. The model Eq. 55 can be simplified by taking $\mathcal{J}_1 = \mathcal{J}_2^*$, which implies that $\rho_1 = \rho_2 = \rho$ and $\tilde{\rho}_1 = -\tilde{\rho}_2 = \rho$. This is a reasonable simplification and will be adopted throughout our analysis.

5. 2D Weyl semimetal

As mentioned above, 2D Weyl semi-metals can be constructed from a lattice model [21]. In this section, we show how it emerges from the porphyrin thin film layer. In the 2D limit $t_{\perp} = t_D = 0$, the Hamiltonian Eq. 55 has the form

$$\begin{aligned} \mathcal{H}(k_{\pm}) = & \rho [\cos(k_+ - \Phi) + \cos(k_- + \Phi)] \sigma_x \\ & - \rho [\cos(k_+ - \Phi) - \cos(k_- + \Phi)] \sigma_y. \end{aligned} \quad (56)$$

For $\Phi = 0$ or π , Eq. 56 can be written as

$$\mathcal{H}_{\Phi=0} = \rho \cos\left(\frac{k_x}{2}\right) \cos\left(\frac{k_y}{2}\right) \sigma_x + \rho \sin\left(\frac{k_x}{2}\right) \sin\left(\frac{k_y}{2}\right) \sigma_y, \quad (57)$$

where $\mathcal{H}_{\Phi=\pi} = -\mathcal{H}_{\Phi=0}$. As shown in Fig. 5, the energy band has four degenerate points located at $\mathbf{W}_1 = (0, \pm\pi)$ and $\mathbf{W}_2 = (\pm\pi, 0)$. However, the degeneracy of an energy band does not guarantee a Weyl semi-metallic phase. To obtain a nontrivial topological semimetal, symmetry consideration must be taken into account. For the Hamiltonian in

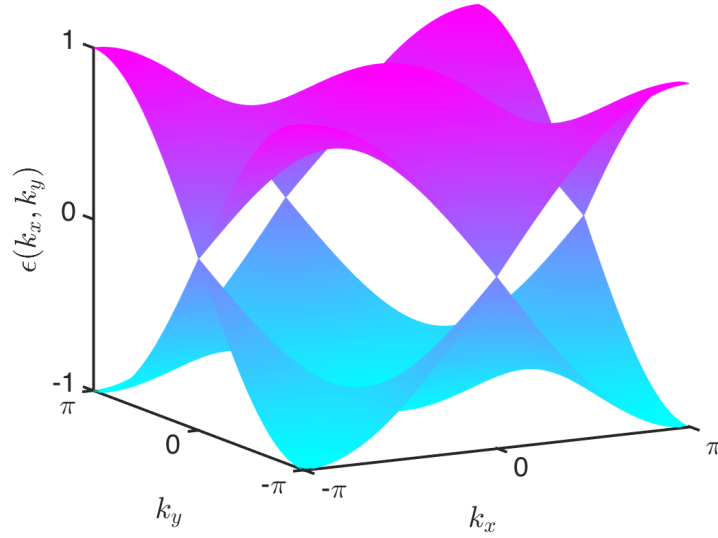


Figure 5. Color online. The energy band of Eq. 57 in units of ρ . There are four degenerate points in the BZ with each pair located at $\mathbf{W}_1 = (0, \pm\pi)$ and $\mathbf{W}_2 = (\pm\pi, 0)$.

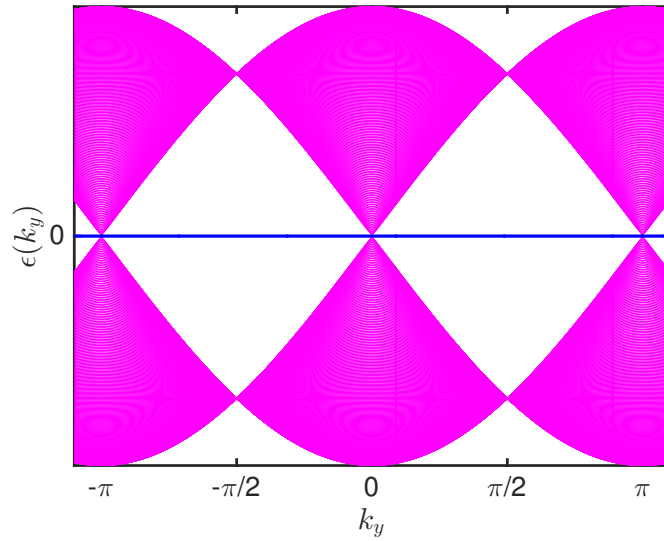


Figure 6. Color online. The bulk energy band (pink) and the chiral edge states (blue) of Eq. 57 along the k_y direction.

Eq. 57, time-reversal symmetry ($\mathbf{k} \rightarrow -\mathbf{k}$; $\boldsymbol{\sigma} \rightarrow -\boldsymbol{\sigma}$) is broken but inversion symmetry ($\mathbf{k} \rightarrow -\mathbf{k}$) is preserved. For 2D systems, however, there is an additional hidden discrete symmetry with an anti-unitary operator [21]. More generally, if a system is invariant under the action of an anti-unitary operator and the square of the operator is not equal to 1, there must be degeneracy protected by this anti-unitary operator [21]. In the present model, there is an anti-unitary operator for which the Hamiltonian (Eq. 57) is invariant. It is given by $\mathcal{U} = \sigma_x \mathcal{K} T_{\hat{x}/2 + \hat{y}/2}$, where \mathcal{K} is complex conjugation and $T_{\hat{x}/2 + \hat{y}/2}$

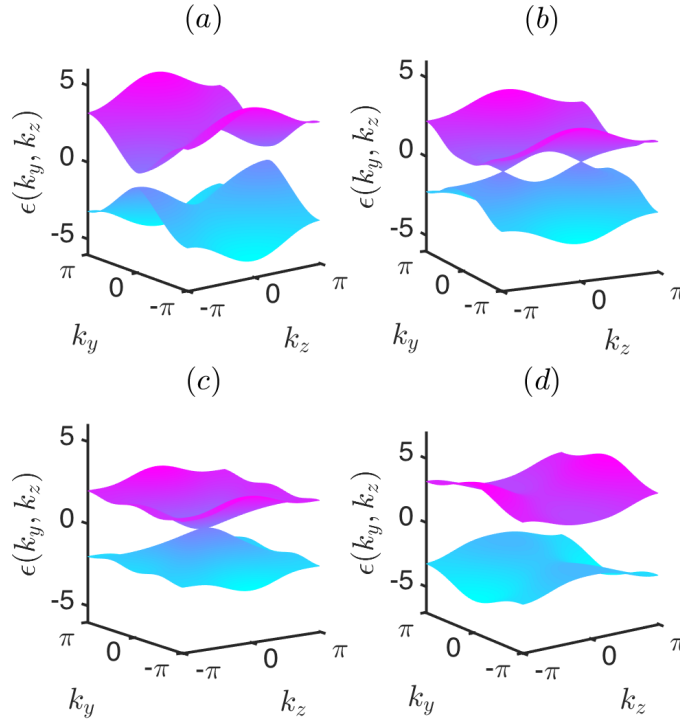


Figure 7. Color online. The evolution of the energy along $k_x = 0$ at $\Phi = \pi/2$ with $\mu_{xy} = 4t_{\perp}$. The four regimes are: the insulating phase (a). $\gamma < \gamma_-$, Weyl semi-metallic phase (b). $\gamma_- < \gamma < \gamma_+$, phase transition point (c). $\gamma = \gamma_+$, and the 3D QAH phase (d). $\gamma > \gamma_+$.

translates the lattice by $\hat{x}/2$ and $\hat{y}/2$ along the x - and y -directions. It is easy to check that $\mathcal{U}^{-1}\mathcal{H}_{\Phi=0}\mathcal{U} = \mathcal{H}_{\Phi=0}$. It follows that $\mathcal{U}^2 = e^{-i(k_x+k_y)} = -1$ at \mathbf{W}_1 and \mathbf{W}_2 . Note that $\mathcal{U}^2 = -1$ at various points in the BZ, e.g., $\mathbf{k} = (\pi/2, \pi/2)$. However, the energy does not vanish at these points, the reason being that they are not \mathcal{U} -invariant points. Thus, the theorem stated above is only valid at the \mathcal{U} -invariant points. The four degenerate points in the energy spectrum is consistent with Nielsen-Ninomiya theorem [31], which states that Weyl points must occur in pair(s) with opposite helicity in a lattice model. Near these points, the Hamiltonian is linearized as

$$\mathcal{H}_1(\mathbf{q}) = v_F[\mp q_y \sigma_x \pm q_x \sigma_y], \quad \mathcal{H}_2(\mathbf{q}) = v_F[\mp q_x \sigma_x \pm q_y \sigma_y], \quad (58)$$

where $\mathbf{q} = \mathbf{k} - \mathbf{W}_{1,2}$ and $v_F = \rho/2$.

The Hamiltonian has the general form $\mathcal{H}(\mathbf{q}) = \sum_{ij} v_{ij} q_i \sigma_j$, where v_{ij} form a 2×2 matrix. The chirality of the Weyl points is given by

$$\chi_{\pm} = \text{sign}(\det[v_{ij}]). \quad (59)$$

From Eqs. 58 and 59 we obtain $\chi_{\pm} = \pm 1$ for the whole system, which signifies the topological nature of the system. As a massless Dirac fermion with chirality, the system above can be regarded as a 2D Weyl semi-metal which hosts a 2D Weyl fermion. In Fig. 5, opposite chirality is assigned to neighbouring Weyl points in

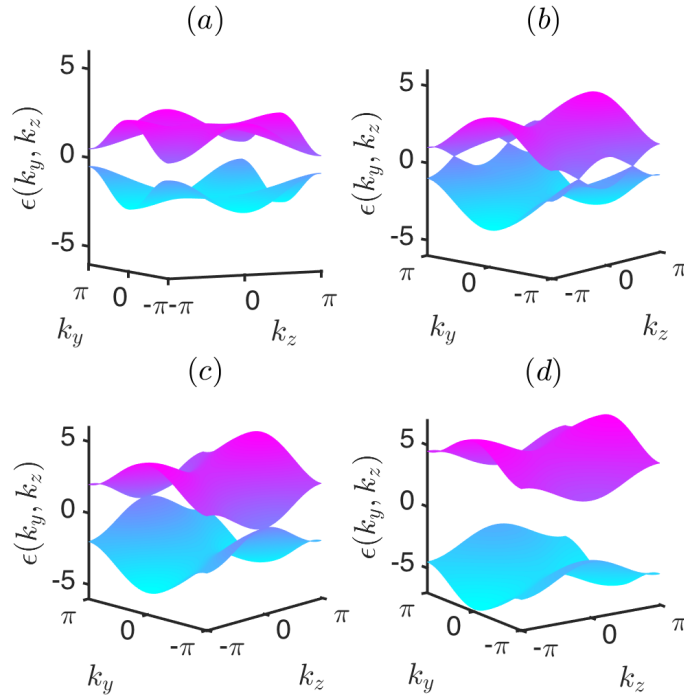


Figure 8. Color online. The evolution of the energy along $k_x = 0$ at $\Phi = 0$ or $\Phi = \pi$ with $\mu_{xy} = 0$. The parameters are the same as Fig. 7.

cyclic order. Moreover, in 2D Weyl semimetal there is a chiral edge state propagating in the intermediate region between the Weyl points. This can be explicitly shown by considering a semi-infinite system with periodic boundary conditions along the k_y direction and open boundary condition along the k_x direction [32]. The bulk band is shown in Fig. 6 along the k_y direction. The bulk gap vanishes at the locations of the Weyl points along the k_y -axis consistent with Fig. 5. However, topological protected flat-band chiral edge states emerge in-between the Weyl nodes. These chiral edge states connect the Weyl points with opposite chirality along the k_y -direction.

6. 3D Weyl semimetal

In this section, we study the possibility of 3D Weyl semi-metallic phase in the proposed lattice model. The goal is to utilize this model to simulate the TI multilayer surface states (Fermi arc). In 3 dimensions we must have $t_D \neq 0$; a 3D Weyl semimetal can be obtained with a judicious choice of Φ . In particular, for $\Phi = \pi/2$ and $\mathcal{J}_1 = \mathcal{J}_2^*$, Eq. 55 has the form $\mathcal{H} = \mathcal{H}_{\Phi=\pi/2} + \mathcal{H}_z$, where

$$\mathcal{H}_{\Phi=\pi/2} = 2v_F \cos\left(\frac{k_x}{2}\right) \sin\left(\frac{k_y}{2}\right) \sigma_x - 2v_F \cos\left(\frac{k_y}{2}\right) \sin\left(\frac{k_x}{2}\right) \sigma_y. \quad (60)$$

$$\mathcal{H}_z = \left[\mu_{xy} - 2t_{\perp}(\cos k_x + \cos k_y) - \frac{t_D}{2} (\cos(k_z d) + \cos(k_W d)) \right] \sigma_z. \quad (61)$$

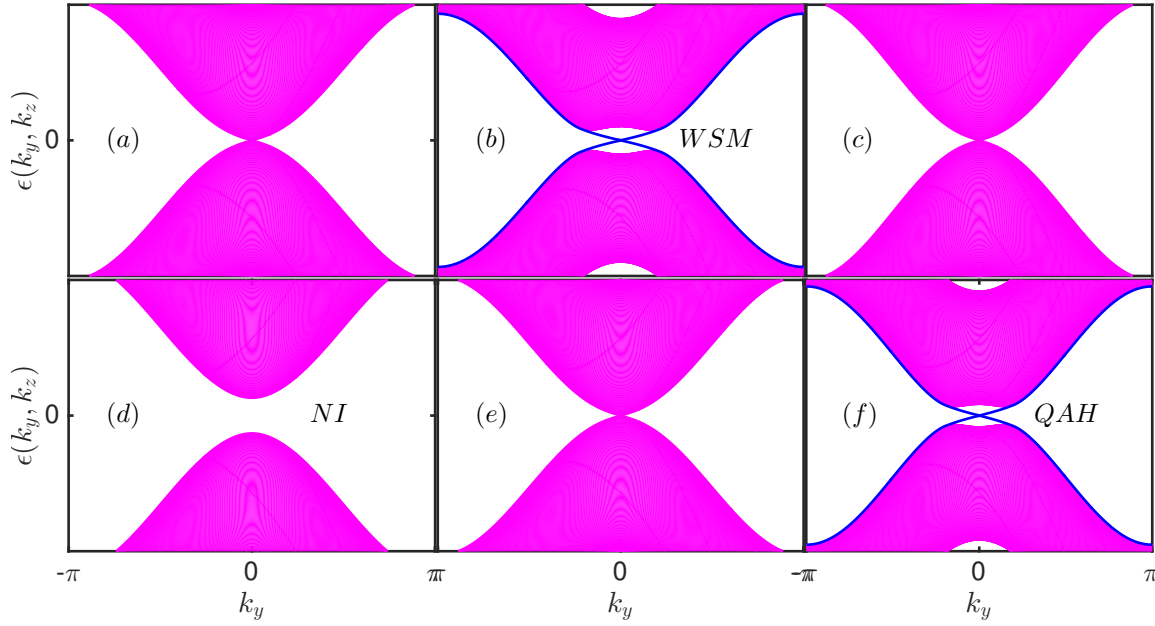


Figure 9. Color online. The bulk energy band and the surface states of Eq. 55 along the k_y direction with several values of k_z with $\Phi = \pi/2$. From (a)–(c), describe a Weyl semi-metallic phase with fine-tuned $\mu_{xy} = 4t_{\perp}$, $t_D = 0.75t_S$, $\gamma_- < \gamma = 0.25t_S < \gamma_+$, $t_{\perp} = t_S = 1$; and k_z varies as $k_z = k_z^-$, $k_z = k_z^-/2$, and $k_z = -k_z^-$ or k_z^+ respectively. From (d)–(f), describe the insulating phases, now $t_{\perp} < 0$ see Eqs. 15 and 16. (d) $\gamma < \gamma_-$ and $k_z = \pi$. (f) $\gamma = \gamma_+$ and $k_z = 0$. (e) $\gamma > \gamma_+$ and $k_z = 0$. See text for explanation.

It is easy to see that with a fine-tuned $\mu_{xy} = 4t_{\perp}$, the partial continuum limit of Eqs. 60 and 61 is exactly the inner 2×2 block of Eq. 6 and the Weyl nodes are located at the same points $\mathbf{W} = (0, 0, k_z^{\pm})$, with $k_z^{\pm} = \pi/d \pm k_W$. Thus, the porphyrin thin film multilayer lattice model recovers that of TI thin film multilayer in the partial continuum limit. The evolution of the energy bands in the BZ are shown in Fig. 7. Near the Weyl points the Hamiltonian is given by

$$\mathcal{H}(\mathbf{q}) = v_F q_y \sigma_x - v_F q_x \sigma_y \mp \tilde{v}_F q_z \sigma_z, \quad (62)$$

where $\mathbf{q} = \mathbf{k} - \mathbf{W}$, and $\tilde{v}_F = t_D d \sin(k_W d)/2$.

The Hamiltonian still has the general form $\mathcal{H}(\mathbf{q}) = \sum_{ij} v_{ij} q_i \sigma_j$, only that v_{ij} is now a 3×3 matrix with components $v_{yx} = v_F$, $v_{xy} = -v_F$, $v_{zz} = \pm \tilde{v}_F$. The chirality of the Weyl points is the same $\chi_{\pm} = \pm 1$. In this case, the nontrivial topology of Eq. 55 stems from the fact that Eq. 55 preserves inversion symmetry but breaks time-reversal symmetry, when $\Phi = \pi/2$. Another judicious choice of Φ is $\Phi = 0$ or π . The resulting Hamiltonian in this case is given by $\mathcal{H} = \mathcal{H}_{\Phi=0} + \mathcal{H}_z$, but it is different from that of TI thin film. However, the system still preserves inversion symmetry and breaks time-reversal symmetry; thus a Weyl semi-metallic phase can be obtained. There are four Weyl points in the BZ, each pair is located at $\mathbf{W}_1 = (0, \pi, \tilde{k}_z^{\pm})$ and $\mathbf{W}_2 = (0, -\pi, \tilde{k}_z^{\pm})$,

where $\tilde{k}_z^\pm = \pi/d \pm \tilde{k}_W$ and $\tilde{k}_W = \frac{1}{d} \arccos[\cos(k_W d) - \tilde{\mu}_{x,y}]$, with $\tilde{\mu}_{x,y} = 2\mu_{x,y}/t_D$. The energy bands are shown in Fig. 8. The Hamiltonian near the Weyl points is a combination of Eq. 58 and the last term in Eq. 62.

Now, we study the surface states evolution of the Weyl semi-metallic phases above. This is an important feature of 3D Weyl semimetals [7, 9] and it is what is observed in most experiments [17, 18, 19, 20]. In our lattice model, these states can be solved explicitly for any surface not perpendicular to the z -axis. In fact, they are nothing but the edge states of the effective 2D model for fixed values of k_z . We have shown the evolution of the states for $\Phi = \pi/2$ in Fig. 9 (a)–(f), which corresponds exactly to the ultra-thin film of TI multilayer studied above. The top panel describes the Weyl semi-metallic phase bounded by two gapless bulk bands at the location of the Weyl points. For $k_z \in (k_z^-, k_z^+)$, there exist dispersive surface states propagating in the vicinity of the bulk gap only when $t_\perp > 0$. They are gapless at $k_y = 0$ exactly at zero energy. In the bottom panel we show the insulating phases after the Weyl nodes annihilate and a gap opens at $k_z = 0$ or $k_z = \pi/d$. In this case, the surface states still capture the appearance of the two insulating phases – 3D QAH and NI only when $t_\perp < 0$. These results are consistent with our previous analysis and the energy dispersion in Fig. 7. For other choices of Φ such as $\Phi = 0, \pi$, the situation is a little bit different. The gapless surface states only occur at $k_y = \pm\pi$, when $k_z \in (\tilde{k}_z^-, \tilde{k}_z^+)$, but $k_y = 0$ is gapped in this case and we observe that there exist gapped surface states propagating in this vicinity (not shown).

7. Conclusion

In this paper, we have presented a detail analysis of two thin film models of Weyl semimetals. We showed that in an ultra-thin film of topological insulator multilayer the parameters of the system can change sign as the system transits from one topological phase to another. In this model, we presented the low-temperature dependence of the chiral magnetic conductivity, induced by a time-dependent magnetic field. We showed that the topological phases of the system can, indeed, be captured by the plateaus of the chiral magnetic conductivity. We also proposed and studied a simple lattice model of porphyrin thin film. We showed that this model embodies many Weyl semi-metallic phases for a specific gauge choice, which acts as a magnetic flux threading the lattice. We obtained a 2D Weyl semi-metallic phase in the σ_x - σ_y space. We showed that the degeneracy of the Weyl nodes is protected by an anti-unitary operator. Our model also realized a 3D Weyl semi-metallic phase, which can be regarded as the lattice model for an ultra-thin film of topological insulator (TI) multilayer. Thus, it paved the way to numerically study the surface states of the TI multilayer. We obtained the edge states and the surface states in two and three dimensions respectively, as well as in all the nontrivial topological phases of the TI multilayer in three dimensions. As the porphyrin thin film is an organic material that can be grown in the laboratory, the proposed model can perhaps be studied experimentally or in 2D optical lattices. As shown in this paper,

the porphyrin thin film is also a candidate to search for chiral relativistic fermions in two dimensions.

Acknowledgement

The author would like to thank J. -M. Hou for enlightening discussions. The author would also like to thank African Institute for Mathematical Sciences for hospitality. Research at Perimeter Institute is supported by the Government of Canada through Industry Canada and by the Province of Ontario through the Ministry of Research and Innovation.

References

- [1] A. A. Burkov and L. Balents, *Phys. Rev. Lett.* **107**, 127205 (2011).
- [2] A. A. Burkov, M. D. Hook, and L. Balents, *Phys. Rev. B.* **84**, 235126 (2011).
- [3] G. B. Halasz and L. Balents, *Phys. Rev. B.* **85**, 035103 (2012).
- [4] A. A. Zyuzin, M. D. Hook, A. A. Burkov, *Phys. Rev. B.* **83**, 245428 (2011).
- [5] A. A. Zyuzin, S. Wu, and A. A. Burkov, *Phys. Rev. B.* **85**, 165110 (2012).
- [6] F. R. Klinkhamer, G. E. Volovik, *Int. J. Mod. Phys. A* **20**, 2795 (2005) ; G. E. Volovik, *The Universe in a Helium Droplet*, Oxford University Press, (2003).
- [7] X. Wan et al., *Phys. Rev. B.* **83**, 205101 (2011).
- [8] S. Murakami, *New J. Phys.* **9**, 356 (2007).
- [9] W. Witczak-Krempa and Y. B. Kim, *Phys. Rev. B.* **85**, 045124 (2012).
- [10] C. -X. Liu, P. Ye, X. -L. Qi, *Phys. Rev. B.* **87**, 235306 (2013); G. Y. Cho, [arXiv:1110.1939](https://arxiv.org/abs/1110.1939).
- [11] K.-Y. Yang, et al., *Phys. Rev. B.* **84**, 075129 (2011).
- [12] C. -Z. Chen, et al., *Phys. Rev. Lett.* **115**, 246603 (2015).
- [13] H. -Z. Lu, S. -B. Zhang, and S. -Q. Shen, *Phys. Rev. B.* **92**, 045203 (2015).
- [14] P. Delplace, J. Li, D. Carpentier, *EPL* **97**, 67004 (2012).
- [15] J.-H. Jiang, *Phys. Rev. A.* **85**, 033640 (2012).
- [16] R. -J. Slager, et al., [arXiv:1509.07705](https://arxiv.org/abs/1509.07705), (2015).
- [17] L. Lu, et al., *Science*, **349**, 622 (2015).
- [18] S. -Y. Xu, et al., *Science*, **349**, 613 (2015).
- [19] B. Q. Lv et al., *Phys. Rev. X* **5**, 031013 (2015).
- [20] B. Q. Lv, et al., *Nature Physics* **11**, 724 (2015).
- [21] J. -M. Hou, *Phys. Rev. Lett.* **111**, 130403 (2013).
- [22] Joel Yuen-Zhou, et al., *Nature Materials* **13**, 1026 (2014).
- [23] H. -Z Lu, et al., *Phys. Rev. B.* **81**, 115407 (2010).
- [24] H. Li, et al., *Phys. Rev. B.* **82**, 165104, (2010).
- [25] H. Li, L. Sheng, and D. Y. Xing, *Phys. Rev. B.* **85**, 045118 2012; *Phys. Rev. B.* **84**, 035310 (2012).
- [26] W. -Y. Shan, H. -Z. Lu, and S. -Q. Shen, *New J. Phys.* **12**, 043048 (2010).
- [27] S. A. Owerre, and J. Nsofini, *Solid State Commun.* **218**, 35 (2015).
- [28] Y. Sakamoto et al., *Phys. Rev. B.* **81**, 165432 (2010).
- [29] Y. Zhang, et al., *Nature*, **6**, 584 (2010).
- [30] F. D. M. Haldane, *Phys. Rev. Lett.* **61**, 2015, (1988).
- [31] H. B. Nielsen and M. Ninomiya, *Phys. Lett.* **105**, 219 (1981).
- [32] X. -L. Qi and S. -C. Zhang, *Rev. Mod. Phys.* **83**, 1057 (2011).
- [33] A. A. Burkov, *Phys. Rev. B* **89**, 155104 (2014).
- [34] D. E. Kharzeev and H. J. Warringa, *Phys. Rev. D* **80**, 034028 (2009).